Nanoscale

PAPER

View Article Online
View Journal

Cite this: DOI: 10.1039/d6nr00776g

Plasmonic glyco-nanoparticles for single-test multiplexed detection and differentiation of cancer cells

A. K. M. Atique Ullah,[a,b] Aniwat Juhong,[b,c] Sherif Ramadan,[a,d] Chia-Wei Yang,[a,b] Zhen Qiu[b,c,e] and Xuefei Huang *[a,b,e]

Precise cancer detection and classification require tools that can readily differentiate normal *vs*. cancerous cells, as well as various types of cancer cells. Herein, we present a plasmonic glyco-nanoparticle (PlasGlyNP) system functionalized with six types of carbohydrates including mannose, galactose, fucose, *N*-acetyl glucosamine, sialic acid, and hyaluronan, to enable multiplex cancer detection and differentiation *via* surface-enhanced Raman scattering (SERS). The particles were colloidally stable under the physiological condition and a variety of stressor conditions. The carbohydrates immobilized on the particles retained their biological recognition selectivities and the particles could sensitively detect carbohydrate binding proteins with the limit of detection down to pM range using SERS. Importantly, a 7-plex PlasGlyNP array generates distinct SERS signatures from a single incubation and measurement per cell type, allowing rapid differentiation of a panel of twelve cell lines, including normal cells and cancer cells with varying metastatic potential, without requiring prior knowledge of specific receptor expression. By enabling simultaneous profiling of multiple glycan–receptor interactions in a single assay workflow, the PlasGlyNP platform provides a versatile tool for interrogating glycan binding profiles relevant to cancer differentiation and detection.

Received 24th February 2026,
Accepted 7th April 2026

DOI: 10.1039/d6nr00776g

rsc.li/nanoscale

Introduction

Cancer remains a leading cause of death globally, characterized by the uncontrolled growth of cells that develop unique molecular signatures distinct from their healthy counterparts. Early and accurate detection of these molecular characteristics can be crucial to guide effective treatment, which has driven the development of various diagnostic methods targeting genetic and protein biomarkers.[1,2] However, many of these approaches rely heavily on prior knowledge of specific biomarkers, which can be limiting as it requires extensive research to establish such biomarkers. The high mutation rates of cancer cells can result in antigenic shifts, potentially leading to false-negative results.[3,4] The heterogeneity and complexity of cancer rendering it challenging to develop reliable detection.[5,6] Therefore, the development of simple and effective techniques to delineate the fine characteristics of cancer cells can have great potential impacts.

Carbohydrates represent a promising class of molecules for cancer cell targeting due to their diverse structures and critical roles in cancer development and disease progression.[7] Aberrant glycosylation and carbohydrate binding of cancer cells have been documented making these interactions important targets for both diagnostics and therapeutics.[8] While carbohydrates present on cell surface can be probed *via* antibodies and/or lectins,[9,10] the ability to profile carbohydrate binding properties of cancer cells by leveraging the binding between carbohydrates and cell surface receptors is attractive, which can provide complementary insights into the molecular landscapes of cancers.[11–14]

To study carbohydrate-receptor interactions, carbohydrates functionalized nanoparticles (glyco-nanoparticles) have become valuable tools.[14–18] Recent advances in glyco-nanoparticle systems have further enabled probing of cancer-associated glycan interactions and cellular phenotyping.[19] While typical carbohydrate-receptor interactions are weak (K_D ~ mM), with their high surface area, glyco-nanoparticles can significantly enhance the avidity of the carbohydrates with the target receptor through multivalent binding.[14,20] In this study, we report the development of a plasmonic glyco-nanoparticle (PlasGlyNP)-based platform for the rapid multiplex detection and differentiation of cancer cells based on their glycan binding abilities.

[a]*Department of Chemistry, Michigan State University, East Lansing, MI, 48824 USA. E-mail: huangxu2@msu.edu*
[b]*Institute for Quantitative Health Science and Engineering, Michigan State University, East Lansing, MI, 48824 USA*
[c]*Department of Electrical and Computer Engineering, Michigan State University, East Lansing, MI, 48824 USA*
[d]*Department of Chemistry, Benha University, Benha 13511, Egypt*
[e]*Department of Biomedical Engineering, Michigan State University, East Lansing, MI, 48824 USA*

Multiplexed molecular detection has been achieved using a variety of analytical platforms, including fluorescence-based labeling, mass spectrometry, and SERS-based approaches. Fluorescence-based multiplexing often relies on spectrally separated fluorophores or sequential labeling strategies, which can limit the number of simultaneously detectable targets due to spectral overlap and photobleaching.[21,22] Mass-spectrometry-based methods provide high molecular specificity and broad molecular coverage but typically require extensive sample preparation and separation steps, making them less suitable for rapid and cell-based screening.[23,24] In comparison, SERS spectra offer intrinsically narrow spectral linewidth that can enable simultaneous detection of multiple targets using spectrally encoded probes.[25,26] Recent advances have further expanded the capabilities of SERS-based multiplexing for highly sensitive and parallel detection of biological targets, including cancer-associated biomarkers and extracellular vesicles.[27–30] These considerations prompted us to investigate the synthesis and applications of PlasGlyNPs for SERS based studies. While glyco-nanoparticles and SERS-based multiplexing have been explored separately, previous glyco-nanoparticle systems typically focus on probing individual glycan–receptor interactions, and conventional SERS multiplexing platforms often rely on separate or sequential measurements of different probes. Their integration into a platform that enables simultaneous, single-test profiling of glycan–receptor interactions without prior biomarker knowledge is underdeveloped. In this work, we address this gap by combining glycan-functionalized nanoparticles with spectrally encoded SERS probes to generate multidimensional phenotypic signatures.

The PlasGlyNP panel consists of surface-enhanced Raman scattering (SERS)-active nanoparticles functionalized with biologically relevant carbohydrates, including mannose (Man), galactose (Gal), fucose (Fuc), *N*-acetyl glucosamine (Glc*N*Ac), and sialic acid (Sia), which collectively represent over 90% of the monosaccharide building blocks of mammalian glycans.[31] In addition, a polysaccharide, *i.e.*, hyaluronan (HA), was also utilized as a coating agent for the PlasGlyNP as HA is known to play important roles in cancer development.[32–34] Here we present a 7-plex PlasGlyNPs SERS array that enables simultaneous profiling of multiple glycan–receptor interactions in a single assay workflow. Distinct SERS signatures generated from a single incubation and measurement allow differentiation between normal and cancerous cells, as well as among cancer cells with differing metastatic potential, without requiring prior knowledge of specific receptor expression (Fig. 1). This approach establishes PlasGlyNP-based SERS multiplexing as a versatile strategy for probing glycan binding profiles relevant to cancer biology.

Results and discussion

Synthesis and characterization of PlasGlyNPs

Among various techniques for detection such as UV-vis absorbance, fluorescence and magnetic resonance imaging, we choose to explore SERS due to its potential for multiplex detection.[25] In this work, multiplex detection refers to the simultaneous interrogation of multiple glycan–receptor interactions within a single experimental workflow using a mixture of spectrally distinct PlasGlyNPs. After screening multiple probes, we synthesized seven SERS NPs (Scheme S1), each bearing a distinct Raman reporter molecule, including mercaptobenzoic acid (MBA), 4-fluorothiophenol (FTP), 2,3,5,6-tetrafluorobenzenethiol (TFBT), 4,4′-dipyridyl (DP), d8-4,4′-dipyridyl (DDP), 4,4′-azobis(pyridine) (ABP), and 2-phenylethanethiol (PET) (Fig. S1a). These Raman reporters were selected due to their characteristic and spectrally distinct SERS signatures, each exhibiting a dominant and non-degenerate marker band that remains resolvable even within spectrally proximal Raman windows. We have previously shown that mixture of SERS NPs could be readily deconvoluted and quantified from the composite spectra.[35] Comparisons of Raman and SERS spectra confirmed the pronounced signal enhancement with SERS NPs and calculated enhancement factors ranging from 4.4×10^5 to 1.06×10^6 (Fig. S1).

For biological and diagnostic applications of NPs, it is crucial that the particles are colloidally stable under biological conditions.[36] While the freshly synthesized SERS NPs gave strong SERS signals, we found that when these particles were dissolved in potassium phosphate (KPB) buffer, their characteristic red color quickly faded with extensive NP aggregates observed. To enhance the NP stability, we investigated coating of NPs with bovine serum albumin (BSA). The disulfide bonds in BSA were first reduced with sodium borohydride to generate free sulfhydryl groups (–SH) forming reduced BSA (rBSA), which upon incubation with SERS NPs, could bind to the NPs through Au–S bonds forming a protective "lying hair" layer (Scheme 1a).[37] The SERS NPs were incubated with 0, 0.05, 0.10, 0.20, 0.40, 1.0, and 2.0 mg mL^{-1} of rBSA respectively (named SERS NP-rBSA0–6). UV-vis spectra of the resulting NPs (Fig. 2a) revealed a gradual red-shift in the plasmon peak of the NPs (Table S1) with increasing rBSA amounts, likely due to the increasing diameters from rBSA coating.[38] SERS spectra (Fig. S2) of SERS NP-rBSA0–6 displayed similar SERS intensities, suggesting rBSA coating did not dampen the SERS signals. This could be attributed to the thin rBSA layer minimizing the dampening effect typically observed with thicker hydrophilic polymers on Au NPs' SERS signals.[37] Incubation of the rBSA coated SERS NPs in KPB buffer showed that with less than 0.20 mg rBSA, significant NP aggregates were formed leading to the loss of the red color of NP solution (Fig. 2b). With 1 mg mL^{-1} or more rBSA, the resulting SERS NPs were most stable as indicated by the color of their KPB solution (Fig. 2b). Furthermore, the stability of the SERS NP coated with 1 mg mL^{-1} rBSA was confirmed by the insignificant changes of their UV-vis (Fig. 2c and d) and SERS spectra (Fig. S2 and Fig. 2e) in buffer.

With stable rBSA coated SERS NPs in hand, we constructed a library of PlasGlyNPs, incorporating five key monosaccharides commonly found in mammalian cell glycomes: Man, Gal, Fuc, Glc*N*Ac, and Sia (Fig. 1). The rBSA coating on the SERS

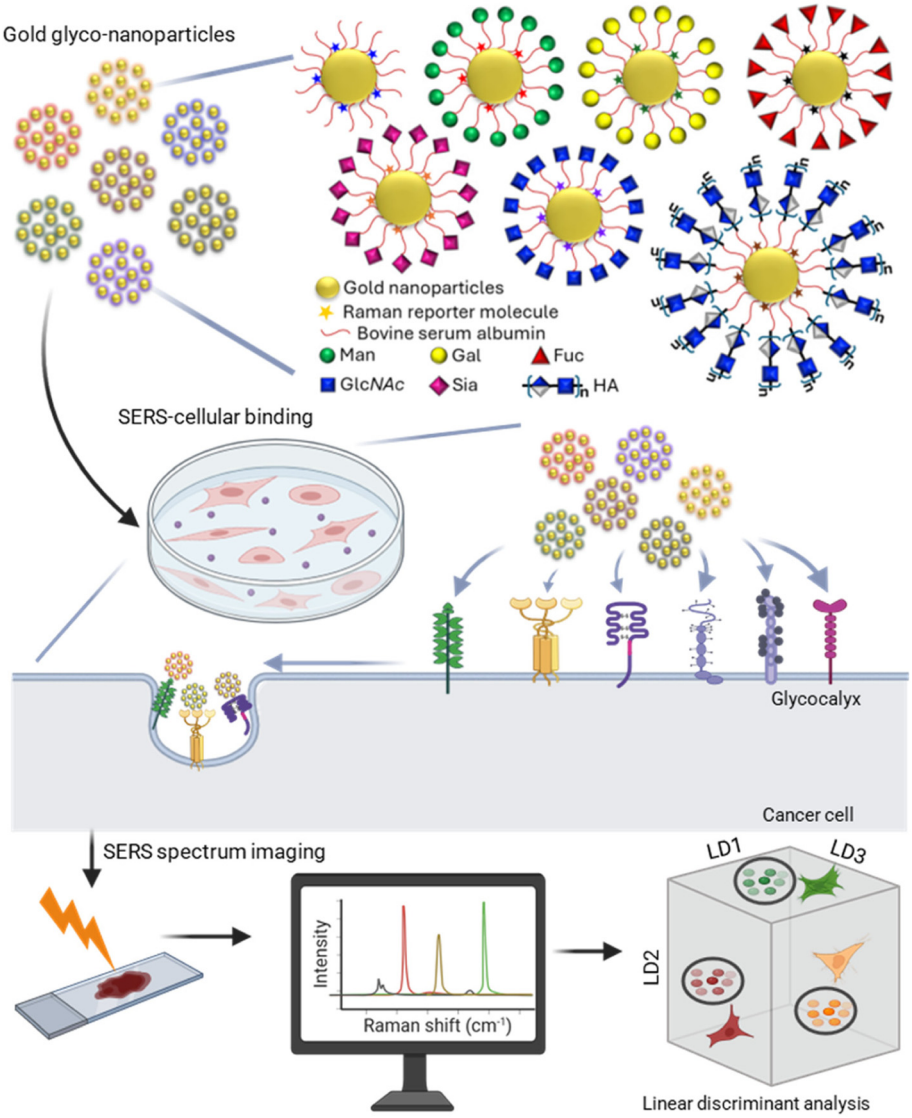

Fig. 1 Schematic representation showing the overall flow of the study. A library of plasmonic glycol-nanoparticles (PlasGlyNPs) was constructed, containing five different monosaccharides (Man, Gal, Fuc, GlcNAc, and Sia) and one polysaccharide, hyaluronic acid (HA), all serving as targeting ligands. Additionally, one type of nanoparticle without sugar moieties was included as a control. The nanoparticles were then screened against different types of cancer cells and normal cell to detect cancer and differentiate between cancer types based on their differential affinity towards PlasGlyNPs.

NPs not only stabilized the particles, but also introduced amine groups on NP surface for carbohydrate functionalization. To prepare the PlasGlyNPs, the requisite monosaccharide ligands were synthesized (Schemes S2–S6), and covalently conjugated with the specific type of rBSA SERS NP (Scheme 1b and c). To optimize the PlasGlyNPs, we functionalized SERS NP-rBSA with various amounts (0.05–2.0 mg mL^{-1}) of the monosaccharide ligand (Table S1). For example, for Fuc installation, concentrations up to 1.0 mg mL^{-1} did not cause any noticeable change in the SERS intensities of rBSA-coated DP SERS NPs (Fig. S3 and Fig. 2f). Therefore, 1.0 mg mL^{-1} Fuc concentration was determined as the optimal amount of fucose used to functionalize rBSA coated DP SERS NP. This protocol was subsequently applied to other monosaccharides without the need for further optimization. The polysaccharide HA was incorporated onto the SERS NP using thiolated HA (Scheme 1d). Furthermore, a SERS NP without any sugar moieties was prepared as a control. The resulting panel of SERS nanoprobes was designated according to its reporter molecule and specific carbohydrate conjugation as MBA SERS NP (Control, no carbohydrate coating), Man-FTP SERS NP, Gal-TFBT SERS NP, Fuc-DP SERS NP, GlcNAc-DDP SERS NP, Sia-ABP SERS NP, and HA-PET SERS NP. The PlasGlyNPs were characterized with a variety of techniques. Transmission electron microscopy (TEM) images of SERS NP indicated that the average diameter of the particles was around 50 nm

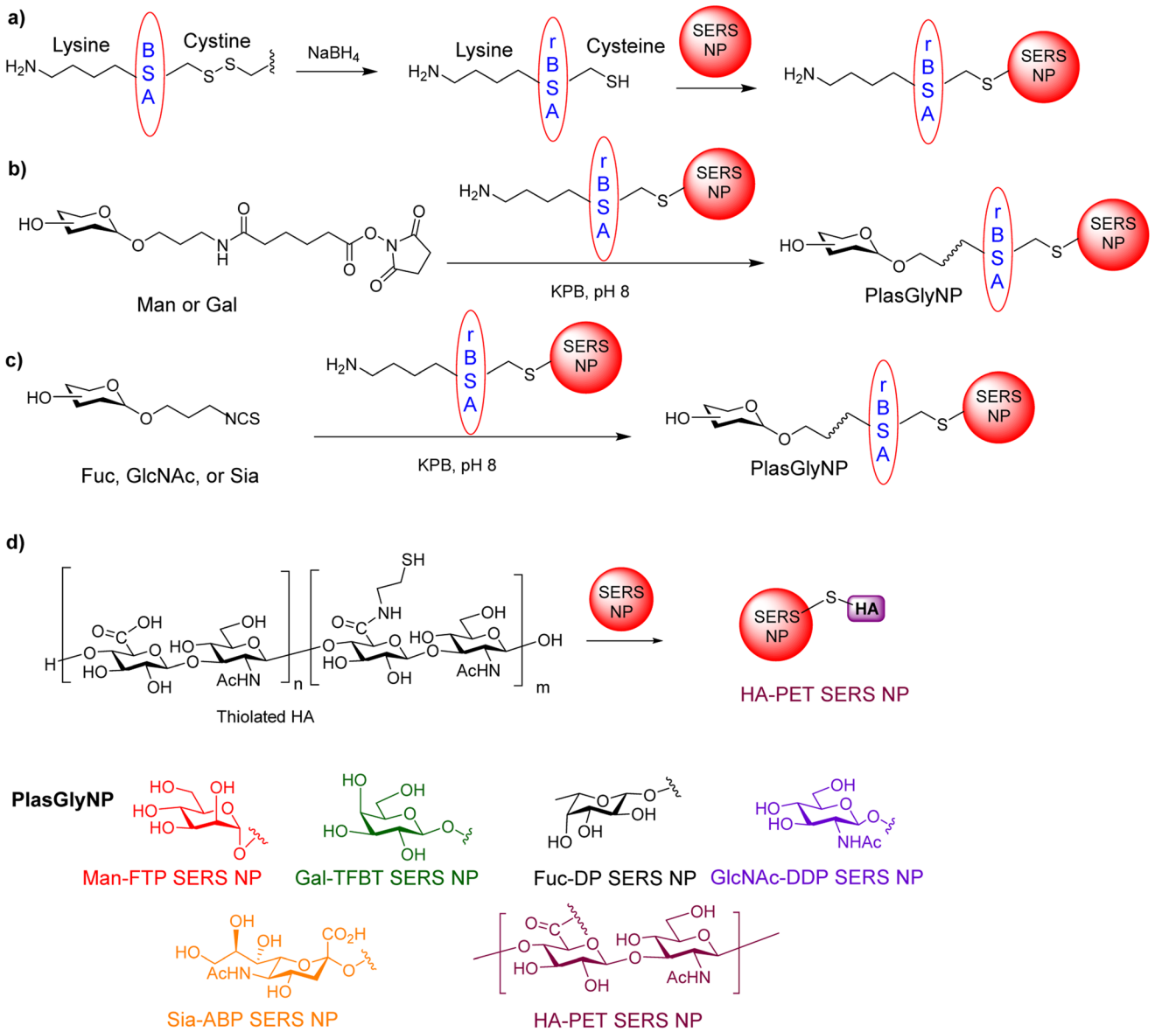

Scheme 1 Synthesis of PlasGlyNPs.

(Fig. S4a).[35] Hydrodynamic size analysis of all NPs (Fig. S4b) showed an increase in particle diameters following rBSA coating and carbohydrate functionalization. Zeta potential measurements (Fig. S4c) showed consistently negative values for all seven uncoated SERS NPs. Upon rBSA coating, the zeta potential values became more positive, presumably due to the amine groups introduced from rBSA.[39,40] The carbohydrate loading level was estimated to be ~1.0×10^{12} monosaccharides per NP. This was achieved by calculating the difference between the amount of carbohydrate used for coating the SERS NPs and the amount of unbound carbohydrate remaining in the supernatant after conjugation based on the anthrone-based colorimetric assay. After carbohydrate functionalization of NPs, the zeta potential values became more negative likely due to the consumption of amines on rBSA for conjugation.[40] Functionalization of SERS NPs with HA resulted in more negative zeta potential values due to HA's inherent negative charges under the physiological condition.[41] In addition to structural characterization, the sensitivity and linearity of the resulting PlasGlyNPs were evaluated to assess their suitability for multiplexed SERS analysis. Calibration curves constructed for each glycan-functionalized probe exhibited excellent linear responses over the tested concentration ranges, with correlation coefficients (R^2) between 0.992 and 0.998 (Fig. S5). For multiplexed experiments, the concentrations of individual PlasGlyNPs were adjusted prior to mixing to yield comparable baseline SERS intensities across probes, ensuring balanced signal contributions and avoiding dominance by probes with higher intrinsic Raman cross-sections.

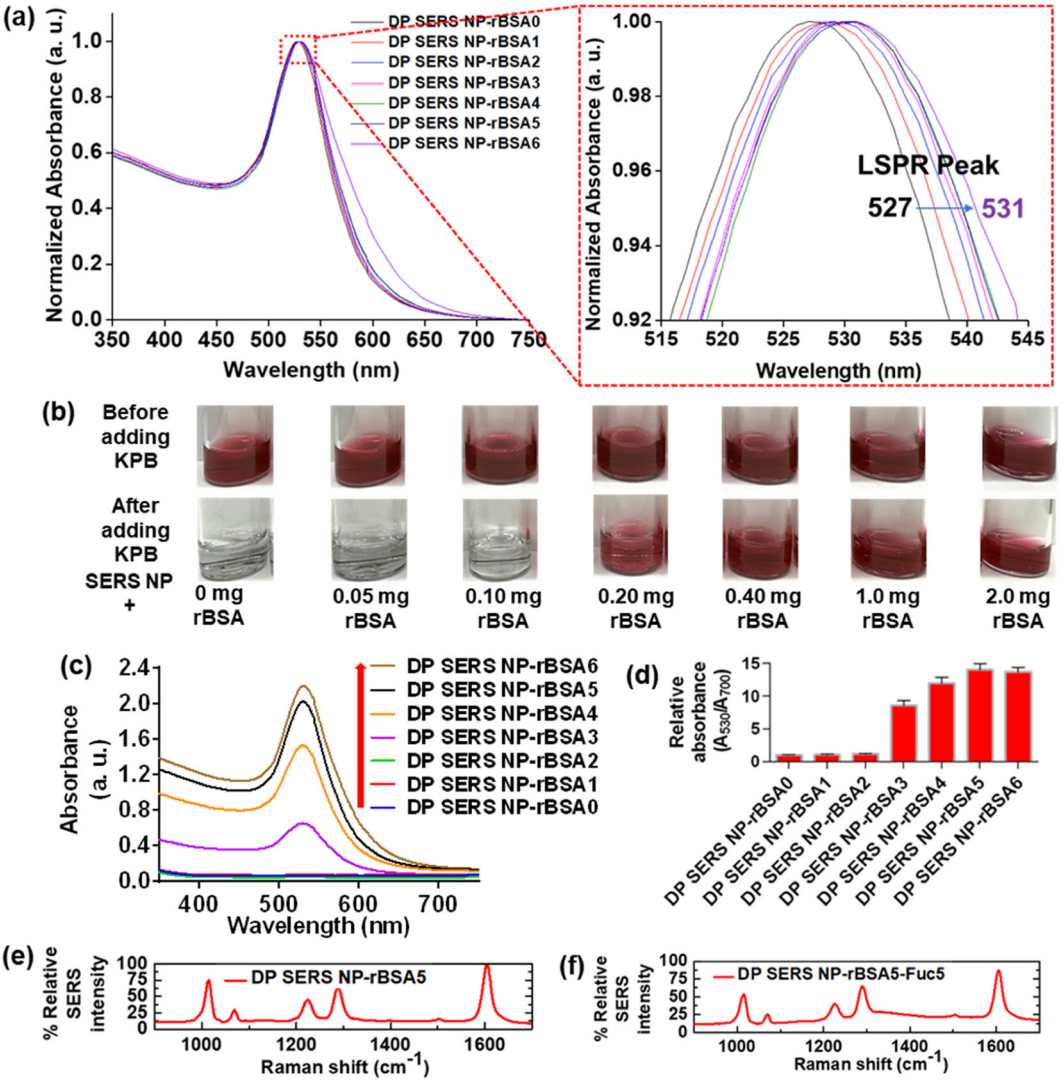

Fig. 2 Physicochemical characterization of PlasGlyNPs. (a) UV-Vis absorbance spectra of DP SERS NP and DP SERS NP-rBSA1–6, with an inset showing a magnified view. The inset highlights the shift in plasmonic absorbance peaks to higher wavelengths as the extent of rBSA coating increases. (b–d) Stability characterization of DP SERS NP-rBSA0–6 in KPB (pH = 8): (b) photograph illustrating color variations, (c) UV-Vis absorption spectra, and (d) relative absorption spectra (data are presented as mean values ± standard deviation, n = 3) indicating that SERS NP-rBSA5 achieves sufficient rBSA coating, thereby protecting the SERS NPs from aggregation. Representative SERS spectra of (e) DP SERS NP-rBSA and (f) DP-SERS NP-rBSA-Fuc.

PlasGlyNPs are colloidally stable against freezing, lyophilization, heating, under physiological and different pH condition

To establish the potential for biological applications, PlasGlyNPs were subject to comprehensive stability assessment[36,42] under a variety of stressor conditions, such as freezing, lyophilization, heating, physiological and different pH conditions (data for Fuc-DP SERS NP are presented as a representative example). To test stability against freeze–thaw, PlasGlyNPs were subjected to multiple cycles of freezing at −80 °C followed by thawing. When the particles were redissolved in water, bare DP SERS NPs exhibited a color change from red to gray and a significance decrease in the intensities of SPR absorbance, reflecting aggregation upon freeze–thaw treatment (Fig. S6a and S6b). In contrast, Fuc-DP SERS NP retained its characteristic red color and surface plasmon resonance (SPR) absorption (Fig. S6c–S6e), thus confirming rBSA-carbohydrate coating was essential for enhanced stability toward freeze–thaw. In lyophilization tests, a solution of Fuc-DP SERS NP was lyophilized to dryness, which was then redissolved. The resulting solution retained its red color and original UV-vis absorption (Fig. S7). However, bare DP SERS NPs severely aggregated after lyophilization, evident by a color change from red to colorless and decreased SPR absorbance upon rehydration (Fig. S7). Particle stability assessments under physiological conditions (pH 7.4, ~137 mM NaCl) were performed next. Bare DP SERS NPs quickly aggregated upon exposure to PBS, evidenced by a color shift and reduced UV-vis

absorbance, while PlasGlyNPs maintained dispersion without color change or aggregation over 24 hours (Fig. S8). Thermal stability testing at 85 °C for 4 hours showed that both PlasGlyNPs and bare NPs retained their red color and SPR absorption, demonstrating their stabilities under heating conditions (Fig. S9). Finally, stability was assessed across a range of pH values (pH 5–9) (Fig. S10). Bare DP SERS NPs remained stable under acidic and neutral conditions but showed pronounced aggregation and loss of SPR absorbance under basic conditions. In contrast, PlasGlyNPs retained their red color and UV–vis absorption throughout the entire pH range tested, confirming excellent tolerance under variable pH environments.

The SERS spectra of PlasGlyNPs were acquired under all the aforementioned stress conditions. Remarkably, no significant changes in SERS intensities of any PlasGlyNPs were observed (Fig. S11), confirming the retention of their plasmonic properties and the absence of aggregation following glycan functionalization. This robust performance of PlasGlyNPs suggests the potential of PlasGlyNPs for biosensing and diagnostic applications, as their functional properties remain intact even under challenging environmental and physiological conditions.

PlasGlyNPs retained carbohydrate binding selectivities

With the PlasGlyNPs in hand, we next tested whether the immobilized carbohydrates maintain their biological recognition. This was accomplished by assessing their binding to lectins including Concanavalin A (Con A), a Man-selective lectin;[43] Bandeiraea simplicifolia isolectin (BS-I), a Gal-selective lectin;[44] Lotus tetragonolobus agglutinin (TPA), a Fuc-selective lectin;[45] and Wheat Germ Agglutinin (WGA), selective for GlcNAc, sialic acid (Sia), and HA,[46–48] *via* colorimetric analysis and SERS detection.

In the colorimetric assay, incubation of PlasGlyNPs and the lectin that can bind with the carbohydrate coating of the NPs resulted in cross-linking and aggregation of the NPs, leading to a measurable decrease in plasmonic absorbance.[49] For example, incubation of Con A (20 μg mL^{-1}) with the PlasGlyNP panel showed a decrease in absorbance or change of the color of the solution only for Man-FTP SERS NP, while all the other PlasGlyNPs without Man coating exhibited negligible absorbance or color changes (Fig. 3a and b). This was consistent with the known binding preference of Man by Con A.[43] To further confirm the specificity, we conducted a competition assay by adding free mannose (0.5 M) to the mixture of Con A/Man-FTP SERS NP. The free mannose competed for Con A binding thus disrupting the Con A/Man-FTP SERS NP complex, restoring plasmonic absorbance and color of the Man-FTP SERS NP (Fig. 3a and b). As minor sample-related variations may affect baseline absorbance, to ensure consistent comparisons, we calculated the relative absorbance ($A_{530\ nm}$/$A_{700\ nm}$), where $A_{530\ nm}$ is the plasmonic peak and $A_{700\ nm}$ is the tail-end absorbance. This ratiometric approach minimizes nonspecific effects and highlights specific changes due to carbohydrate–lectin-induced nanoparticle aggregation. The changes in relative absorbance (Fig. 3c) further confirmed the specificity of the interaction.

To enhance the rigor of the analysis, other lectins including BS-I, TPA, and WGA were utilized. As a Gal selective lectin, BS-I demonstrated strong binding only to Gal-TFBT SERS NP as evident from the changes in color upon addition of BS-I, which could be competitively inhibited by adding free galactose (Fig. S12a–S12c). The incubation with BS-I had little

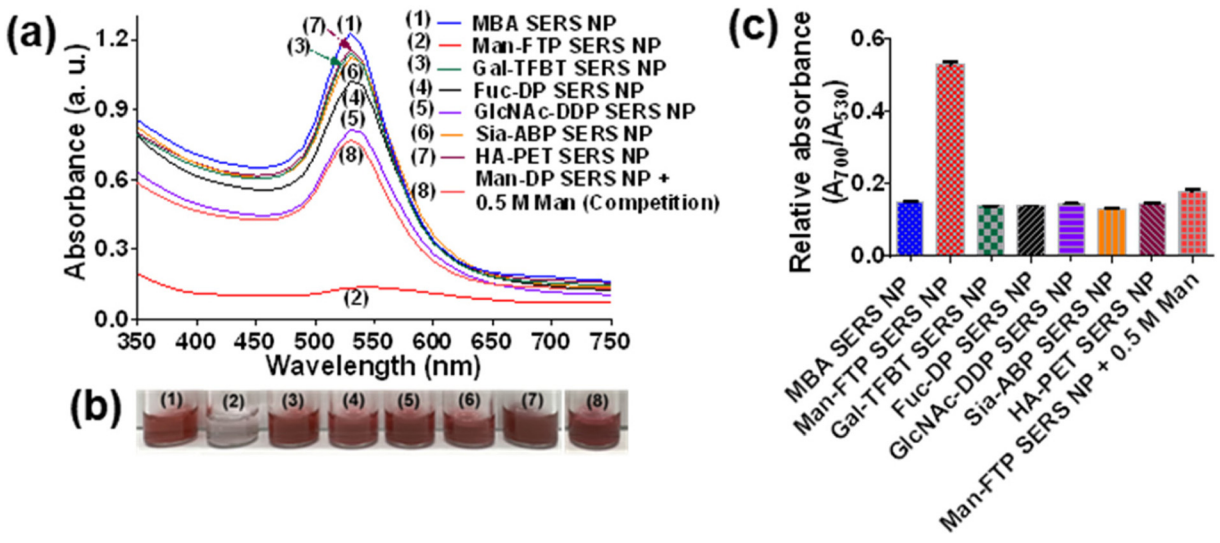

Fig. 3 (a) Plasmonic absorption spectra of PlasGlyNPs after incubation with Con A (20 μg mL^{-1}). (b) Corresponding colorimetric images captured by a digital camera. (c) Relative absorbance values derived from the visible spectra (data are presented as mean values ± standard deviation, n = 3). Among the tested nanoparticles, Man-FTP SERS NP exhibited a strong response to the mannose-selective lectin Con A, confirming selective glycan–lectin interaction. No cross-reactivity was observed with other nanoparticles. The binding was competitively inhibited by the presence of excess free mannose, supporting the selectivity of the interaction.

effects on color and SPR band intensities of other PlasGlyNPs. In a similar manner, Fuc selective lectin TPA selectively bound to Fuc-DP SERS NP (Fig. S12d–S12f), while WGA showed preferential binding towards GlcNAc-DDP SERS NP, Sia-ABP SERS NP, and HA-PET SERS NP (Fig. S12g–S12i), consistent with their known carbohydrate affinities. Notably, control MBA SERS NP, devoid of surface carbohydrates, showed no changes in plasmonic absorbance when incubated with any of the lectins, suggesting minimal nonspecific protein binding to the nanoparticle surface. These results demonstrate that PlasGlyNPs retain their biological recognition preferences as the corresponding free carbohydrate in solution.

With the ability to selectively bind with the lectin established for PlasGlyNPs, we next tested the limit of detection of lectins (Fig. 4). In the colorimetric assay, upon incubation with increasing concentrations at micromolar concentrations of the binding lectin Con A, the plasmonic absorbance of a solution of Man-FTP SERS NP decreased linearly (Fig. 4a(ii), b and c), which is attributed to the cross-linking of Man-functionalized NPs by the tetrameric Con A, leading to aggregation. In contrast, control NP, which lacks Man, displayed no change in absorbance across Con A concentrations tested, underscoring the specificity of the mannose–Con A interaction. The limit of detection (LOD) for Con A using this colorimetric method was

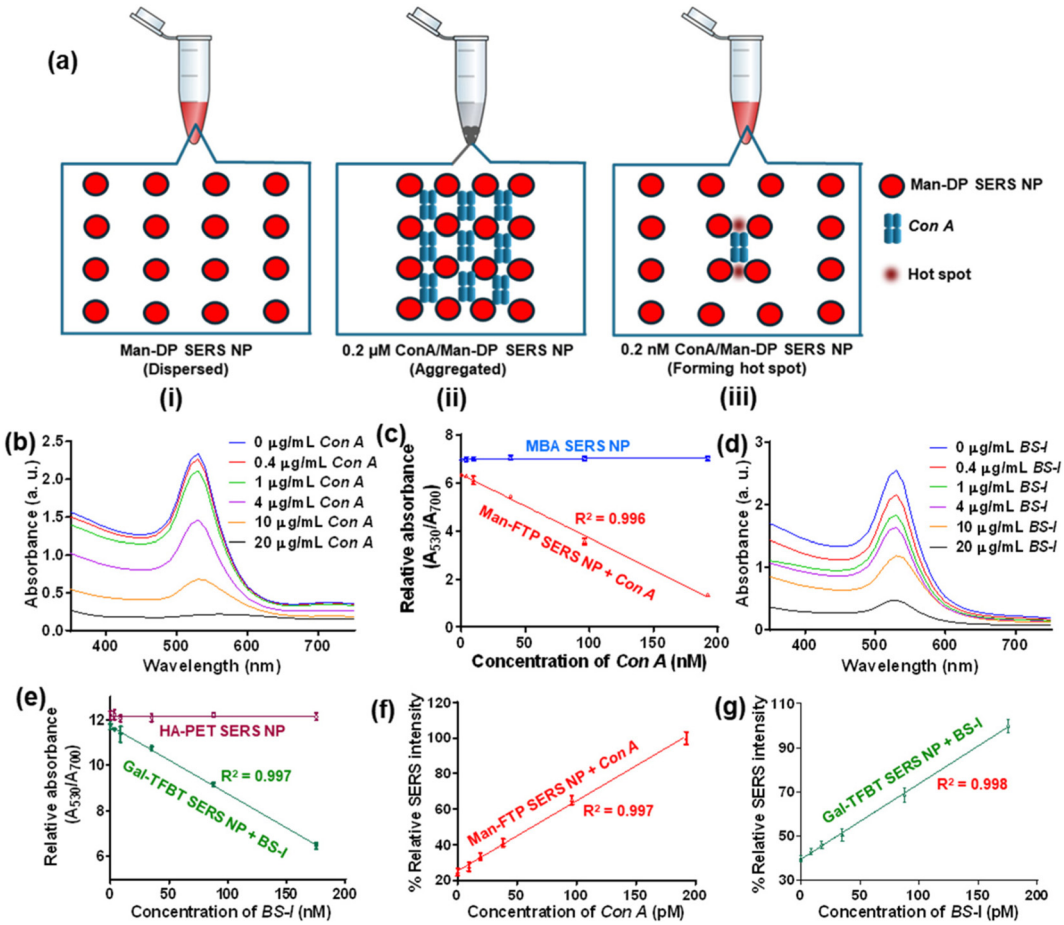

Fig. 4 (a) Proposed binding mechanisms of Man-FTP SERS NP with Con A at different concentrations: (i) Man-FTP SERS NP are well-dispersed in water; (ii) incubation with micromolar concentration (0.2 μM) of Con A, a mannose-selective tetrameric lectin, induces aggregation, resulting in decreased plasmonic absorbance, and (iii) incubation with picomolar (200 pM) of Con A creates plasmonic hot spots, enhancing SERS intensity. (b) Plasmonic absorbance spectra of Man-FTP SERS NP (200 pM) at increasing Con A concentrations in the micromolar range, showing decreased absorbance with higher Con A levels, confirming binding. (c) Relative plasmonic absorbance of Man-FTP SERS NP and carbohydrate-free MBA SERS NP (both at 200 pM) upon incubation with increasing micromolar concentrations of Con A. Man-FTP SERS NP shows a linear decrease in absorbance, indicating binding, while MBA SERS NP remains unchanged. (d) Representative plasmonic absorbance spectra of Gal-TFBT SERS NP (200 pM) with increasing micromolar concentrations of BS-I, showing decreased absorbance, confirming binding. (e) Relative plasmonic absorbance of Gal-TFBT SERS NP and nonbinding HA-PET SERS NP (both at 200 pM) with increasing micromolar concentrations of BS-I. Gal-TFBT SERS NP shows a linear absorbance decrease, while HA-PET SERS NP remains unchanged. (f) SERS intensity of Man-FTP SERS NP (200 pM) upon incubation with increasing nanomolar concentrations of Con A, demonstrating a linear intensity increase due to hot spot formation. (g) SERS intensity of Gal-TFBT SERS NP (200 pM) upon incubation with increasing nanomolar concentrations of BS-I, showing a linear intensity increase due to specific interaction and hot spot formation. Relative absorbance data are presented as mean values ± standard deviation, n = 3; % relative SERS intensity data are presented as mean values ± standard deviation, n = 5.

8 nM, representing around five to ten folds of improvement over the previously reported LOD value of 40–80 nM.[50,51] The limit of detection was obtained by calculating as 3σ ($\sigma = S_0/S$); S_0, standard deviation of the blank sample; S, the slope of the calibration curve.[52] Similarly, BS-I binding to Gal-TFBT SERS NP led to a decrease in plasmonic absorbance with increasing BS-I concentrations (Fig. 4d) and a linear correlation between BS-I concentration and relative absorbance (Fig. 4e). Non-binding NPs, such as HA-PET SERS NP, incubated with BS-I, showed no significant changes in absorbance, further validating the specificity of each lectin–carbohydrate interaction. For BS-I, our assay achieved an LOD of 20 nM.

SERS measurements can be another method for detection besides the colorimetric assay. Interestingly, we observed that incubation of the PlasGlyNPs with low concentrations (pM to nM) of Con A resulted in higher SERS intensities as compared to PlasGlyNP alone. This is attributed to the formation of plasmonic hot spots due to binding of PlasGlyNPs by the corresponding lectin, without inducing large-scale aggregation (Fig. 4a(iii)).[51] To confirm that this SERS signal enhancement resulted from specific binding, we incubated Man-FTP SERS NP and Gal-TFBT SERS NP with BS-I and Con A respectively (Fig. S13 and S14). Only Con A induced a noticeable increase in SERS intensity of Man-FTP SERS NP (Fig. S13), indicating selective binding. In comparison, Gal-TFBT SERS NP showed noticeable SERS intensity enhancement upon incubation with BS-I but not with Con A (Fig. S14), confirming selective Gal-BS-I binding. However, the SERS enhancement efficiency among different glycosylated PlasGlyNPs varies, which is likely related to differences in glycan–lectin interaction strength and binding geometry. These factors can influence cross-linking efficiency, nanoparticle organization, and interparticle coupling during early-stage clustering. As a result, the formation and quality of localized plasmonic hot spots are modulated, leading to differences in SERS signal enhancement. Quantification of SERS intensity showed a linear correlation between Con A concentration and SERS intensity for Man-FTP SERS NP (Fig. 4f), as well as between BS-I concentration and SERS intensity for Gal-TFBT SERS NP (Fig. 4g). The SERS-based LOD for Con A was determined to be ~15 pM, which is around three times more sensitive than the previously reported SERS-based LOD value.[51] Similarly, for BS-I, we achieved an LOD of ~12 pM. Notably, the SERS-based LOD is in the picomolar (pM) range —approximately 1000 times more sensitive than that obtained (nM) from the corresponding colorimetric assay. The pM sensitivity achieved for lectin detection using SERS is directly relevant to the subsequent cell-binding studies. Cell-surface carbohydrate-binding receptors are often expressed heterogeneously and at low effective local densities, particularly across different cell types and disease states. The ability of PlasGlyNPs to detect lectin–glycan interactions at pM concentrations suggests that the platform possesses sufficient sensitivity to resolve subtle differences in glycan–receptor interactions when applied to more complex biological systems. This level of sensitivity establishes that the analytical performance of the PlasGlyNPs is not a limiting factor for downstream cell-binding analyses.

Reproducibility of nanoparticle synthesis is an important consideration for nanoparticle-based sensing systems. In this study, PlasGlyNPs were prepared using a consistent synthetic procedure, and the resulting nanoparticles exhibited stable SERS spectral features across independent measurements. The reproducibility of SERS signals observed across multiple replicates supports the reliability of the nanoparticle probes under the experimental conditions used in this work. While batch-to-batch variability was not systematically evaluated in this study, the consistent spectral behavior suggests that the synthesis yields particles with reproducible SERS properties.

Analysis of mammalian cell binding profiles with PlasGlyNPs *via* SERS multiplexing

Following successful lectin detection, we assessed the potential of PlasGlyNPs for mammalian cell binding and detection through SERS. Carbohydrates serve as recognition elements that probe cell-surface carbohydrate receptors, complementing antibody-based methods.[53] Unlike antibodies, which detect specific antigens present in certain cancer cells, carbohydrate ligands provide a broader recognition spectrum across various cell types.[54] This versatility enables reduced reagent requirements by facilitating the monitoring of multiple cell types using a single panel of ligands.[55] While glyco-NPs have been utilized to monitor cell binding detected through fluorescence, absorbance or magnetic resonance imaging,[15,56–58] these methods have relatively low throughput, requiring measurements of each NP individually with each cell type. In comparison, with the PlasGlyNPs, the binding of the full array of NPs with one cell type could be measured in a single experiment.

As a proof-of-concept demonstration in a controlled biological system, we studied a library of 12 types of cells. This includes one normal breast cell line (MCF10A) and eleven representative cancer cell lines: IMR-32 (neuroblastoma), Capan-2 (pancreatic), MCF7 (breast), MDA-MB-231 (breast), HepG2 (liver), SKOV-3 (ovarian), SK-MEL-28 (melanoma), MC38M1 (colon), HeLa (cervical), HL-60 (leukemia), and A549 (lung). Each cell type was incubated with the mixture of seven SERS NPs (six PlasGlyNP types along with the control nanoparticle MBA SER NP without carbohydrate coating). Following the removal of unbound particles, SERS spectra of the cells were acquired. The amounts of each type of NP bound to the cells were determined following deconvolution of the composite SERS spectra obtained from each cell line (Fig. 5). The ability to resolve partially proximal reporter bands in the composite spectrum was experimentally verified using spectra acquired from mixed probes.[35] The Raman bands are narrow with full width at half maximum of the peaks at 14–20 cm^{-1}. Thus, even closely spaced marker bands such as those from ABP (1160 cm^{-1}), DDP (1195 cm^{-1}), and MBA (1122 cm^{-1}) can be readily distinguishable under our acquisition and fitting conditions (Fig. S15).

Cancer cells gave diverse responses to each SERS-NP encoded with a unique SERS reporter molecule. The control NP exhibited negligible SERS intensity for all cell lines (Fig. 5). In contrast, significant SERS intensities were observed across

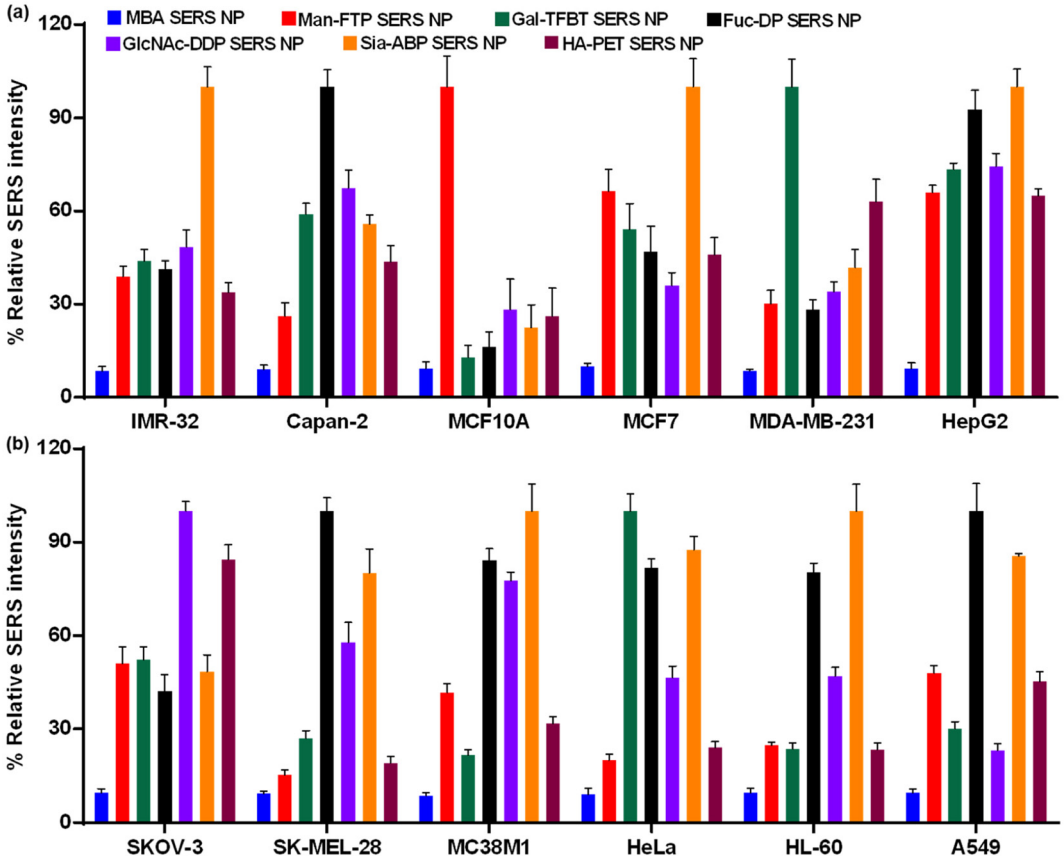

Fig. 5 Systematic screening of PlasGlyNPs with a panel of 12 types of cells. Relative percentage SERS intensities were measured after incubating all seven PlasGlyNPs together with 12 different cell line. The relative % SERS intensity was calculated by dividing the SERS intensity of each PlasGlyNP by the highest SERS intensity within the corresponding GlyNP category and multiplying by 100. Each data point represents the average of ten individual measurements with error bars indicating standard deviations.

the 12 cell lines following incubation with PlasGlyNPs (Fig. 5) suggesting binding and retention of NPs by cells. Analysis of SERS signals revealed diverse responses between the cells and specific PlasGlyNPs. MDA-MB-231 and HeLa cells interacted strongly with Gal-DP SERS NP, consistent with previously reported high levels of galectins, a family of Gal-binding lectins on these cell lines.[59,60] MCF10A cells showed interactions with Man-SERS NP, suggesting active Man receptors, while SKOV-3 cells demonstrated strong binding to GlcNAc and HA, aligning with prior reports of high GlcNAc and HA receptor expression in this cell line.[61,62] Most cell lines examined in our study displayed binding with Fuc-DP SERS NP and Sia-ABP SERS NP (Fig. 5), suggesting the expression of Fuc and Sia receptors on these cells.[57] While the observed binding patterns are consistent with reported receptor expression profiles, the present study focuses on phenotypic sensing rather than direct mechanistic validation. Future work involving receptor blocking, knockdown, or enzymatic glycan modification will further elucidate the molecular mechanisms underlying these interactions.

While this study employs well-defined cultured cell lines to enable controlled evaluation of glycan–cell interactions, real biological samples such as heterogeneous cell populations or tissue specimens present additional complexity that may influence nanoparticle binding behavior. Therefore, the present work serves as a proof-of-concept for multiplexed glycan profiling, and future studies will extend this platform to more complex biological systems, including mixed cell populations and clinically relevant samples, to further assess its translational potential.

This profiling of sugar-binding preferences provides valuable insights into cancer biology and enables improved characterization of carbohydrate receptor interactions. This approach represents a shift from traditional single-biomarker detection toward multidimensional glycan interaction profiling, enabling phenotypic classification of cells based on their collective binding behavior. Compared to previously reported glyco-nanoparticle sensing systems[63] and SERS multiplexing platforms,[30] the present approach enables simultaneous and single-test profiling of multiple glycan–cell interactions, providing a more efficient and information-rich strategy for cell phenotyping.

To independently validate the SERS-derived binding profiles, nanoparticle association with cells was further quantified using inductively coupled plasma–optical emission spectroscopy (ICP-OES). As a representative example, MCF7 cells

were incubated with the highest-binding Sia-ABP SERS NP and the lowest-binding GlcNAc-DDP SERS NP under identical conditions. Following thorough washing to remove unbound nanoparticles, the cellular gold content was quantified by ICP-OES (Fig. S16). The results revealed a significantly higher gold uptake for cells treated with Sia-ABP SERS NP compared to GlcNAc-DDP SERS NP, in good agreement with the relative binding trends observed by SERS. This orthogonal elemental analysis confirms that the SERS signal differences reflect genuine variations in nanoparticle association with cells rather than spectral artifacts.

Discrimination between cancerous and normal cells using unique SERS signatures

The PlasGlyNP array provides a facile single-test approach to distinguish cell types including normal *vs.* cancerous cells through their unique SERS signatures. Here, the term "single-test" refers to the simultaneous interrogation of multiple glycan–receptor interactions using a single incubation of cells with a mixed PlasGlyNP array, followed by one SERS measurement for each cell type, rather than implying the absence of standard incubation or washing steps. For example, clear differences in glycan binding patterns were observed comparing MCF10A, a model for normal breast epithelial cells, with MCF7 and MDA-MB-231 breast cancer cells (Fig. 6). MCF10A was selected as a well-established, non-tumorigenic human breast epithelial cell line that is widely used as a reference model in comparative breast cancer studies. Accordingly, conclusions regarding differences between normal and cancerous breast cells in this work are drawn within this defined experimental proof-of-principle framework. The SERS signals from the Man-FTP SERS NP on MCF10A cells were significantly higher than those from both MCF7 and MDA-MB-231 (P < 0.0001), indicating a greater expression of Man-binding receptors in MCF10A. Conversely, Gal binding was significantly lower (P < 0.0001) in MCF10A compared to both MCF7 and MDA-MB-231. This trend may be attributed to the elevated expression of galectin-3 and galectin-1 in cancerous cells, where these receptors play critical roles in promoting cell–matrix interactions involved in cancer progression.[64,65] While these results demonstrate the capability of the PlasGlyNP platform to distinguish normal and cancerous phenotypes in a proof-of-principle manner, broader generalization to other normal cells will require validation using additional cell types, which will be the focus of future studies. These findings underscore the effectiveness of PlasGlyNPs as a single-test detection tool that can differentiate normal cells from cancerous phenotypes through glycan-binding signatures.

Besides cancer *vs.* normal cells, PlasGlyNPs are capable of distinguishing cancer cells with differential metastatic phenotypes. MCF7 and MDA-MB-231 cells were selected as representative models of less metastatic and highly metastatic breast cancer phenotypes, respectively, based on extensive prior experimental characterization of their invasive and metastatic behaviors *in vitro* and *in vivo*.[66,67] In comparing less-metastatic MCF7 cells with highly metastatic MDA-MB-231 cells, distinct

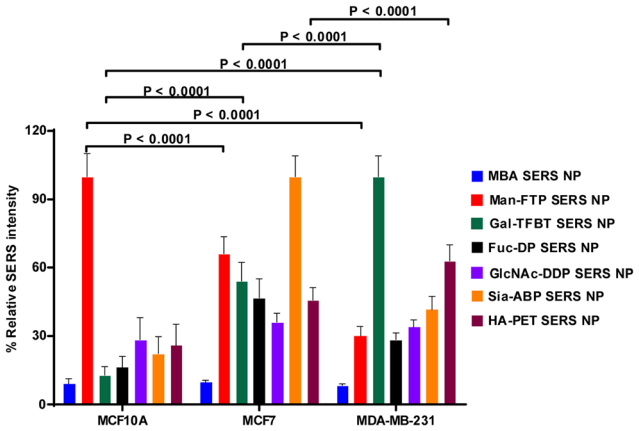

Fig. 6 Differentiation between normal, cancerous, and metastatic cells using PlasGlyNPs based on unique SERS signatures. Comparison of glycan-binding patterns between normal breast epithelial cells (MCF10A) and cancer cells (MCF7 and MDA-MB-231) reveals significantly higher mannose binding in MCF10A and increased galactose binding in MCF7 and MDA-MB-231 (P < 0.0001). Differentiation between low-metastatic (MCF7) and highly metastatic (MDA-MB-231) cancer cells shows significantly greater hyaluronic acid (HA) and galactose binding in MDA-MB-231 compared to MCF7 (P < 0.001). These results highlight the ability of PlasGlyNPs to distinguish normal, cancerous, and metastatic cells through unique glycan-binding signatures. Each data point represents the average of ten individual measurements with error bars indicating standard deviations. Statistical analysis was performed using GraphPad and statistical significance between two groups was assessed using two-way ANOVA.

differences in glycan receptor interactions were observed (Fig. 6). Hyaluronan (HA) binding was markedly greater by MDA-MB-231 cells than by MCF7 (P < 0.001), likely due to the overexpression of HA receptors CD44 and/or receptor for hyaluronan-mediated motility (RHAMM) in highly metastatic cells.[68,69] Similarly, Gal binding was significantly higher in MDA-MB-231 compared to MCF7, consistent with elevated galectin-1 and galectin-3 levels in metastatic cells.[70,71] These glycan-specific SERS signatures, captured by PlasGlyNPs, underscore their utility as a powerful multiplexing tool for assessing metastatic potential. Here, the observed differences are interpreted as correlative indicators of metastatic behavior rather than direct mechanistic evidence of receptor expression or function.

Establishing SERS-based molecular signatures for differentiating twelve cell lines using linear discriminant analysis (LDA)

With the diverse SERS signature data, we next tested the possibility of distinguishing all 12 cell lines based on their responses to the six types of PlasGlyNPs. To accomplish this, we employed LDA, a statistical technique for group classification that converts SERS intensity values from each cell line into canonical linear discriminants (LDs). These LDs are weighted combinations of the original data optimized for maximizing group separation.[72–74] LDA was performed using individual replicate measurements rather than averaged data to

preserve intrinsic variability and avoid artificial clustering effects. For LDA, each independent SERS measurement was treated as an individual observation rather than using cell-line–averaged spectra. Specifically, SERS intensity data corresponding to the six PlasGlyNPs were collected from 10 independent measurements per cell line, yielding a total of 120 observations across 12 cell lines, resulting in a 120 × 6 data matrix (control nanoparticle excluded). All statistical analyses were performed using the Statistical Package for the Social Sciences (SPSS), a widely used statistical software for data analysis. Excitingly, the analysis produced distinct LDs, successfully clustering all the 12 cell lines into 12 distinct groups (Fig. 7). This clustering demonstrates that the variations in SERS intensity within the PlasGlyNP array function as unique molecular signatures, enabling clear differentiation across cell lines.

To validate the robustness of our classification, we employed multiple validation techniques. First, a leave-one-out cross-validation (prediction group analysis) in SPSS confirmed 100% accuracy for both the original and cross-validated cases (Table S2). In this approach, each observation was iteratively treated as an independent test sample, providing a stringent validation particularly suitable for datasets of moderate size, where independent validation sets are limited, and effectively allowing each data point to serve as a test case within the validation framework.[75,76] This high accuracy reflects the reliability of our LDA model. Additionally, the confusion matrix (Table S3) provided further confirmation, showing that each cell line was correctly classified into its respective cluster with 100% accuracy, emphasizing the effective differentiation power of our SERS signatures. Finally, we conducted a Wilks' Lambda analysis to evaluate the statistical significance of each discriminant function (Table S4). The low Wilks' Lambda values and highly significant Chi-square tests ($p < 0.001$) for each function affirm the contribution of each discriminant function to the group separation, enhancing the reliability of our LDA results. Given the dataset size, the use of leave-one-out cross-validation, together with confusion matrix and Wilks' Lambda analysis, provides a rigorous assessment of model robustness and minimizes the likelihood of overfitting. Together, these findings confirm that despite the relatively simple structures of the monosaccharides and HA used, the SERS intensity variations within the PlasGlyNP array can be utilized as distinct molecular signatures for each cell line, enabling reliable differentiation across the 12 cell lines. This analysis demonstrates the potential of our approach for precise classification and identification of cancer cell lines.

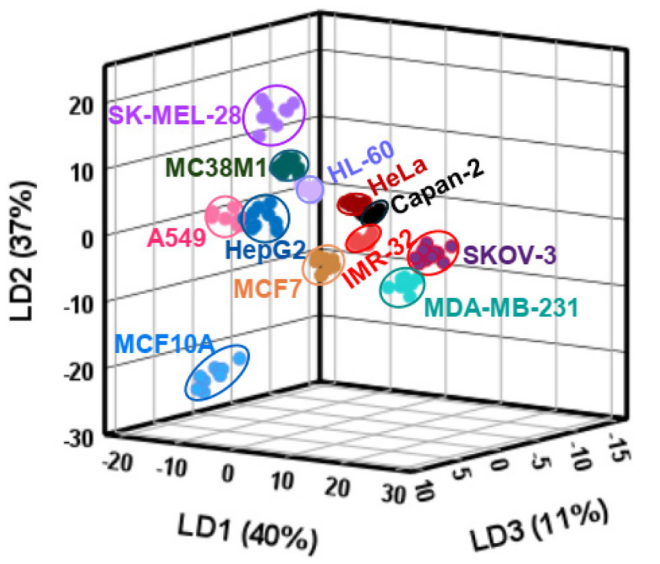

Fig. 7 LDA plots showing the first three linear discriminants (LDs) derived from replicate level SERS intensity data obtained using the PlasGlyNPs array across 12 different cell lines. Each point represents an independent measurement (n = 10 per cell line), and ellipsoids indicate the distribution of replicates within each group. Complete differentiation of all 12 cell lines was achieved.

Confirmation of cellular interaction and biocompatibility of PlasGlyNPs

To confirm cellular interactions of PlasGlyNPs with cells, we performed transmission electron microscopy (TEM) and scanning electron microscopy (SEM) coupled with energy-dispersive X-ray spectroscopy (EDX) analyses of cells. MCF7 cells were incubated with either Sia-ABP SERS NP, which led to significant SERS signals to cells, or MBA SERS NP, which did not generate significant SERS signals. The cellular incubation was followed by thorough washing of the cells with PBS to remove unbound nanoparticles. TEM analysis of cells treated with Sia-ABP SERS NP revealed numerous electron-dense structures confined within membrane-bound vesicles, suggesting cellular uptake and selective vesicular entrapment of the nanoparticles (Fig. S17). These vesicles are consistent with endosomal or lysosomal compartments typically involved in nanoparticle trafficking.[77,78] To further validate this observation, high-magnification TEM images were obtained from both experimental and control conditions. Vesicles containing Sia-ABP SERS NPs were clearly observed (Fig. 8a–c), whereas cells incubated with MBA SERS NP showed no such electron-dense features within vesicular structures (Fig. 8d–f), demonstrating sialic acid dependent internalization of NPs by MCF7 cells. To assess nanoparticle distribution across broader cellular areas and further confirm intracellular localization, SEM-EDX analysis was performed on MCF7 cells treated with Sia-ABP SERS NPs. SEM imaging revealed multiple electron-dense regions dispersed throughout the cytoplasm (Fig. S18a), indicating widespread nanoparticle uptake. EDX spectra collected from eight distinct intracellular locations (Spectra 1–8) consistently detected strong gold (Au) signals (Fig. S18b), providing confirmation of intracellular nanoparticle presence. No Au was detected in other areas of the cells.

Finally, as a test of biocompatibility of the PlasGlyNPs, we conducted cell viability assays of PlasGlyNPs. Man-FTP SERS NP, Gal-TFBT SERS NP, and Sia-ABP SERS NP were incubated with MCF10A, MDA-MB-231, and HepG2 cells, due to the NPs' high binding to these cells respectively. The viabilities of the cells upon PlasGlyNP incubation were compared to untreated

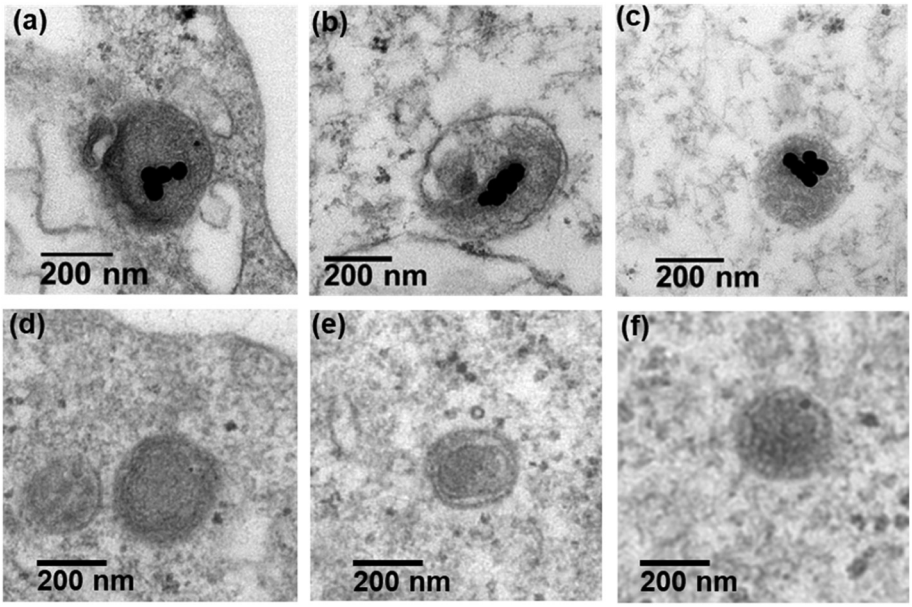

Fig. 8 Representative TEM images of intracellular vesicles in MCF7 cells after incubation with (a–c) Sia-ABP SERS NP and (d–f) MBA SERS NP, followed by thorough washing to remove unbound particles. Dark electron-dense signals indicate that Sia-ABP SERS NP are distinctly localized within vesicular compartments (a–c), whereas MBA SERS NP are largely absent from vesicles (d–f). These results highlight the selective uptake and preferential vesicular trapping of Sia-ABP SERS NP in cells consistent with the significant SERS signal changes observed with Sia-ABP SERS NP incubated with MCF7 cells. In comparison, no NPs were observed in MBA SERS NP treated cells, which is consistent with the lack of changes of SERS signals from the cells.

controls using the 3-(4,5-dimethylthiazol-2-yl)-5-(3-carboxymethoxy phenyl)-2-(4-sulfophenyl)-2*H*-tetrazolium (MTS) cell viability assay. No significant reduction in cell viability was observed for all cells under the conditions examined (Fig. S19).

Conclusions

We developed a PlasGlyNP platform capable of precise cancer detection, screening, and glycan profiling through SERS multiplexing with a single test per cell line. By functionalizing nanoparticles with 6 types of carbohydrates, this PlasGlyNP array generated distinct SERS signatures upon incubation with a range of cell lines, enabling accurate classification of normal and cancerous cells, as well as differentiation between cancer stages based on metastatic potential. These findings underscore the diagnostic potential of PlasGlyNPs as a powerful tool for revealing glycan-mediated cell surface interactions, which are critical to cancer progression and metastasis. The unique glycan-binding profiles identified for each cell type not only deepen our understanding of cancer cell's glyco-codes but also highlight the potential of this platform in advancing cancer diagnostics and profiling.

Using LDA,[57,79] we demonstrate that SERS signals generated by these PlasGlyNPs serve as distinct molecular signatures, allowing for the precise classification of twelve different cell lines. Validation studies confirm the robustness and accuracy of the method. The PlasGlyNP strategy does not require prior knowledge of the specific receptor present on tumor cell surface, which can help expedite diagnostic studies, and provide an alternative to the "lock-key" bio-recognition paradigm.[80] These PlasGlyNPs are a powerful tool for single-test cancer detection and glycan profiling with the potential to advance non-invasive diagnostics and personalized cancer therapy by revealing critical cell surface interactions.

Experimental

Materials

Trisodium citrate dihydrate ($C_6H_5Na_3O_7{\cdot}2H_2O$, 99.0%), tris base ($NH_2C(CH_2OH)_3$, 99.9%), gold(III) chloride trihydrate ($HAuCl_4{\cdot}3H_2O$, 99.995%), mercaptobenzoic acid, 4-fluorothiophenol, 2,3,5,6-tetrafluorobenzenethiol, 4,4′-dipyridyl, d8-4,4′-dipyridyl, 4,4′-azobis(pyridine), 2-phenylethanethiol, sodium borohydride ($NaBH_4$), and bovine serum albumin were purchased from Sigma Aldrich. Deionized (DI) water (Milli-Q grade, Millipore) with a resistivity of 18.2 MΩ cm was used throughout the experiment.

Synthesis of SERS NPs

All glassware and stir bars used in the synthesis of SERS NPs were cleaned with aqua regia prior to use. SERS NPs were synthesized using a tris-base assisted, seed-mediated method.[35] First, 17 nm AuNP seeds were prepared by boiling 48 mL of MilliQ water in a pre-cleaned 250 mL Erlenmeyer flask. Once boiling, 0.5 mL of 25 mM $HAuCl_4$ and 1.5 mL of 1% sodium citrate were added sequentially to initiate AuNP formation,

indicated by a color change within the first 5 minutes, with stirring continued for an additional 8 minutes to complete the reaction. For the 50 nm SERS NPs, 91 mL miliQ water was boiled, then 4 mL of 0.1 M tris base, 3 mL of the 17 nm seed solution, and 1 mL of 25 mM $HAuCl_4$ were added, resulting in further nanoparticle growth. After 3 minutes, 10 μL of 100 mM Raman dye was added to the reaction mixture, which was stirred for 1 minute, then rapidly cooled in an ice bath. The solution was centrifuged at 5000*g* for 10 minutes at 4 °C, and the SERS NPs were redispersed in miliQ water. Batch-to-batch consistency of SERS NPs was qualitatively verified by comparing baseline SERS intensities from independently synthesized batches, which showed no noticeable differences within experimental variability.

Synthesis of PlasGlyNPs

To prepare PlasGlyNPs, SERS NPs were coated with rBSA to enhance stability and functionality. Reduction of BSA was achieved by dissolving 0.5 g of BSA in 50 mL of miliQ water, adjusting the pH to 7.2, and adding 5% sodium borohydride solution (0.25 g in 5 mL miliQ water). This reaction mixture was stirred for 3 hours, after which the pH was increased to 8.9 to ensure the reduction of disulfide linkages yielding rBSA. The resulting rBSA was purified through ultrafiltration using a 10 kDa molecular weight cutoff (MWCO). For coating, 500 μL solutions of 200 pM SERS NPs in water were mixed with varying concentrations of rBSA (0–2 mg mL^{-1}) and incubated overnight at room temperature. Afterward, unbound rBSA was removed through ultrafiltration with a 100 kDa MWCO membrane by washing twice with water, and rBSA-coated SERS NPs were redispersed in water. The functionalized monosaccharides (Man, Gal, Fuc, GlcNAc, and Sia) were subsequently conjugated to the SERS NP-rBSA complex. To accomplish this, 500 μL of the SERS NPs-rBSA solution (200 pM in KPB, pH = 8) was mixed with monosaccharide solutions (0–2 mg mL^{-1}) and incubated overnight at room temperature. For HA conjugation, thiolated HA (Creative PEGWorks), was directly incubated with SERS NPs without pre-functionalization with rBSA. Unbound carbohydrate ligands were removed by centrifugation followed by washing with miliQ water. The final SERS NP conjugates were redispersed in miliQ water and stored at 4 °C for future applications.

Quantification of carbohydrate loading on PlasGlyNPs

The carbohydrate loading on PlasGlyNPs was quantified using an anthrone-based colorimetric assay. After completion of the carbohydrate conjugation reaction, the nanoparticle suspension was centrifuged to separate the nanoparticles from the supernatant containing unbound carbohydrates. The concentration of unbound carbohydrates in the supernatant was determined using the anthrone assay, with mannose as a calibration standard. Briefly, 100 μL of standard mannose solutions (0, 5, 10, 20, 50, and 100 μg mL^{-1}) or sample supernatant was transferred into a 2 mL glass vial. Subsequently, 200 μL of freshly prepared anthrone reagent (0.5% w/v anthrone in concentrated H_2SO_4) was added slowly at room temperature with thorough mixing. The reaction mixture was then heated at 100 °C for 10 minutes to allow color development. After heating, the samples were cooled to room temperature. The absorbance was measured at 620 nm using a UV–Vis spectrophotometer. A calibration curve was constructed using mannose standards, and the carbohydrate concentration in the samples was determined accordingly. The amount of carbohydrate immobilized on the nanoparticle surface was calculated as the difference between the initial carbohydrate amount and the unbound carbohydrate measured in the supernatant. Based on the nanoparticle concentration, the number of carbohydrate molecules per nanoparticle was estimated.

Characterization of PlasGlyNPs

UV-vis spectra were recorded using a SpectraMax M3 plate reader to assess the optical properties of the synthesized nanoparticles. The hydrodynamic size of the nanoparticles was measured by dynamic light scattering (DLS), and the surface charge (ζ potential) was determined using a Zetasizer Nano ZS apparatus (Malvern, UK). TEM images were captured on a JEOL 1400Flash at an accelerating voltage of 100 kV. SEM images were captured in a JEOL 7500 F (field emission emitter) in STEM mode using transmitted electron detector. EDX was performed using an Oxford instruments Aztec system using a 150 mm^2 silicon drift detector. The concentration of the SERS NPs was calculated following the protocol reported previously.[35] Raman measurements were conducted with a HORIBA Raman spectrometer equipped with a 785 nm excitation laser (35 mW power, 1 s exposure time, and 5 accumulations) to evaluate the SERS response. Gold concentrations were quantified on an ICP-OES from Varian (Model Varian 710).

Dispersion stability against freeze–thaw cycle

Colloidal solutions of PlasGlyNPs and bare SERS NPs (SERS NPs without rBSA and carbohydrate functionalization) were placed in glass vials (0.5 mL, 200 pM, in water), which were frozen at −80 °C for 30 min and then thawed at room temperature for 10 min. The thawed solutions were analyzed using UV–vis and Raman spectroscopy.

Dispersion stability against lyophilization

Colloidal solutions of PlasGlyNPs and bare SERS NPs were transferred in glass vials (0.5 mL, 200 pM in water), which were frozen by placing them in liquid nitrogen for a few minutes and then connected immediately to a freeze-drier (−86 °C) with an applied vacuum (0.03 mbar) for ∼24 h. The freeze-dried products were reconstituted with deionized water (0.5 mL). The NP solutions were analyzed using UV–vis and Raman spectroscopy.

Dispersion stability against heating

Colloidal solutions of PlasGlyNPs and bare SERS NPs were taken in glass vials (0.5 mL, 200 pM in water). The vials were capped to prevent evaporation of water and subsequently were heated for 4 h at 85 °C. They were subsequently analyzed using UV–vis and Raman spectroscopy.

Dispersion stability against a PBS buffer solution

Colloidal solutions of PlasGlyNPs and bare SERS NPs were added in glass vials (0.5 mL, 200 pM in water). A 0.1 mL phosphate-buffered saline (PBS) solution (pH = 7.4, KCl = 2.6 mM, KH_2PO_4 = 1.47 mM, NaCl = 137.9 mM) was added to each vial. UV–vis and Ramans spectroscopic measurements were taken before and after the addition of the PBS solution.

Dispersion stability at different pH values

Colloidal solutions of PlasGlyNPs and bare SERS NPs (0.5 mL, 200 pM in water) were adjusted to different pH values (pH – 10) using appropriate volumes of 0.1 M HCl or 0.1 M NaOH. The solutions were incubated for 24 h at room temperature, and their dispersion stability was evaluated by monitoring UV–vis absorption and Raman spectra.

Cell culture

The IMR-32, Capan-2, MCF10A, MCF7, MDA-MB-231, HepG2, SKOV-3, SK-MEL-28, HeLa, HL-60, and A549 cell lines were obtained from the American Type Culture Collection (ATCC; Manassas, VA, USA). The MC38 cell line was purchased from Kerafast Inc. IMR-32, HepG2, SK-MEL-28, and HeLa cells were cultured in Eagle's Minimum Essential Medium (EMEM) supplemented with 10% heat-inactivated fetal bovine serum (FBS) and 1% penicillin/streptomycin. Capan-2 and SKOV-3 cells were maintained in McCoy's 5A medium supplemented with 10% heat-inactivated FBS and 1% penicillin/streptomycin. MCF10A cells were cultured in DMEM/Ham's F-12 medium supplemented with 5% horse serum, 100 ng mL^{-1} cholera toxin, 20 ng mL^{-1} epidermal growth factor (EGF), 10 μg mL^{-1} insulin, 500 μg mL^{-1} hydrocortisone, and 1% penicillin/streptomycin. MCF7 cells were cultured in Dulbecco's Modified Eagle Medium (DMEM) supplemented with 10% heat-inactivated FBS and 1% penicillin/streptomycin. MDA-MB-231 cells were cultured in Leibovitz's L-15 medium with 10% heat-inactivated FBS and 1% penicillin/streptomycin. HL-60 cells were maintained in RPMI 1640 medium supplemented with 10% heat-inactivated FBS and 1% penicillin/streptomycin. A549 cells were cultured in Ham's F-12K medium with 10% heat-inactivated FBS and 1% penicillin/streptomycin. All cell lines were incubated at 37 °C in a humidified chamber with a 5% CO_2 atmosphere, except for MDA-MB-231 cells, which were maintained in atmospheric conditions as required for L-15 medium.

Cytotoxicity of PlasGlyNPs

The cytotoxic effects of various PlasGlyNPs against normal and cancer cell lines were investigated using MTS cell viability assay established previously.[35]

In vitro SERS multiplexing study

Cells were incubated in a 6 well plate (1×10^6 cells per well) for 6 hours with a mixture of seven SERS probes, comprising six PlasGlyNPs and one control SERS NP, with similar SERS intensities for each probe (~25% Relative SERS intensity) (Fig. S17). Following incubation, cells were washed twice with PBS to remove any unbound nanoparticles. The cells were then resuspended in 100 μL of PBS and mixed thoroughly. A 10 μL aliquot of the cell suspension was placed on an alumina coverslip for SERS analysis. SERS spectra were recorded using a Raman spectrometer equipped with a 785 nm laser and a 10× objective lens. The relatively low-magnification lens was intentionally chosen to provide a larger spot size (~3–4 μm), enabling spectra collection from whole cells rather than restricted subcellular regions. This ensured that the measured signals reflected overall nanoparticle binding profiles at the cellular level. For each 10 μL drop of the suspension, ten independent measurements were collected to ensure reproducibility. The SERS intensity for each nanoparticle type was determined from the highest intensity peak corresponding to its unique Raman reporter molecule: mercaptobenzoic acid (MBA), 1122 cm^{-1}; 4-fluorothiophenol (FTP), 1072 cm^{-1}; 2,3,5,6-tetrafluorobenzenethiol (TFBT), 881 cm^{-1}; 4,4′-dipyridyl (DP), 1605 cm^{-1}; d8-4,4′-dipyridyl (DDP), 1195 cm^{-1}; 4,4′-azobis(pyridine) (ABP), 1160 cm^{-1}; and 2-phenylethanethiol (PET), 1001 cm^{-1}.

Author contributions

Conceptualization: XH, AKMAU. Investigation: AKMAU, AJ, SR, CWY. Data curation: AKMAU. Supervision: XH, ZQ. Funding acquisition: XH, ZQ. Writing – original draft: AKMAU. Writing – review & editing: all authors.

Conflicts of interest

The authors declare no competing interests.

Data availability

The data supporting this article have been included as part of the supplementary information (SI). Supplementary information: all supporting figures, schemes, tables and NMR spectra. See DOI: https://doi.org/10.1039/d6nr00776g.

Acknowledgements

We are grateful for the financial support from National Institutes of Health (R01CA225105 and R35GM158263 to XH), the National Science Foundation (Grants 1808436, 1918074, 2306708, and 2237142-CAREER to ZQ), the Department of Energy (DOE) (Grant 234402 to ZQ), and Michigan State University.

References

1 D. Hanahan and R. A. Weinberg, *Cell*, 2011, **144**, 646–674.
2 C. L. Sawyers, *Nature*, 2008, **452**, 548–552.

3 M. J. Duffy and J. Crown, *Clin. Chem.*, 2008, **54**, 1770–1779.
4 M. Gerlinger and C. Swanton, *Br. J. Cancer*, 2010, **103**, 1139–1143.
5 F. Danhier, O. Feron and V. Préat, *J. Controlled Release*, 2010, **148**, 135–146.
6 M. K. Yu, J. Park and S. Jon, *Theranostics*, 2012, **2**, 3–44.
7 S. Hakomori, *Proc. Natl. Acad. Sci. U. S. A.*, 2002, **99**, 10231–10233.
8 S. S. Pinho and C. A. Reis, *Nat. Rev. Cancer*, 2015, **15**, 540–555.
9 D. H. Dube and C. R. Bertozzi, *Nat. Rev. Drug Discovery*, 2005, **4**, 477–488.
10 N. Sharon, *Biochem. Soc. Trans.*, 2008, **36**, 1457–1460.
11 C.-H. Whang, J. Hong, D. Kim, H. Ryu, W. Jung, Y. Son, H. Keum, J. Kim, H. Shin, E. Moon, I. Noh, H.-E. Lee and S. Jon, *Adv. Mater.*, 2022, **34**, 2203993.
12 I. Zare, S. Z. H. Kiadeh, A. Varol, T. Ö. Varol, M. Varol, S. Sezen, A. Zarepour, E. Mostafavi, S. Z. Nasab, A. Rahi, A. Khosravi and A. Zarrabi, *J. Controlled Release*, 2024, **371**, 158–178.
13 K. Arora, P. M. Sherilraj, K. A. Abutwaibe, B. Dhruw and S. L. Mudavath, *Int. J. Biol. Macromol.*, 2024, **268**, 131511.
14 M. Kalita, M. M. Payne and S. H. Bossmann, *Nanomedicine*, 2022, **42**, 102542.
15 X. Chen, O. Ramström and M. Yan, *Nano Res.*, 2014, **7**, 1381–1403.
16 P. J. Hernando, S. Dedola, M. J. Marín and R. A. Field, *Front. Chem.*, 2021, **9**, 668509.
17 K. El-Boubbou and X. Huang, *Curr. Med. Chem.*, 2011, **18**, 2060–2078.
18 N. C. Reichardt, M. Martín-Lomas and S. Penadés, *Chem. Soc. Rev.*, 2013, **42**, 4358–4376.
19 A. K. M. A. Ullah and X. Huang, *Carbohydr. Res.*, 2026, **559**, 109757.
20 C. Müller, G. Despras and T. K. Lindhorst, *Chem. Soc. Rev.*, 2016, **45**, 3275–3302.
21 J. W. Lichtman and J.-A. Conchello, *Nat. Methods*, 2005, **2**, 910–919.
22 T. Zimmermann, *Adv. Biochem. Eng./Biotechnol.*, 2005, **95**, 245–265.
23 J. Zaia, *Mass Spectrom. Rev.*, 2004, **23**, 161–227.
24 N. H. Packer, C.-W. von der Lieth, K. F. Aoki-Kinoshita, C. B. Lebrilla, J. C. Paulson, R. Raman, P. Rudd, R. Sasisekharan, N. Taniguchi and W. S. York, *Proteomics*, 2008, **8**, 8–20.
25 Y. Wang, B. Yan and L. Chen, *Chem. Rev.*, 2013, **113**, 1391–1428.
26 X. Qian, X. Zhou and S. Nie, *Nat. Biotechnol.*, 2008, **26**, 83–90.
27 C. Duffield, L. M. R. Gomez, S. C. Tsao and Y. Wang, *Nanoscale*, 2025, **17**, 3635–3655.
28 L. Vázquez-Iglesias, G. M. S. Casagrande, D. García-Lojo, L. F. Leal, T. A. Ngo, J. Pérez-Juste, R. M. Reis, K. Kant and I. Pastoriza-Santos, *Bioact. Mater.*, 2024, **34**, 248–268.
29 N. Lyu, A. Hassanzadeh-Barforoushi, L. M. R. Gomez, W. Zhang and Y. Wang, *Nano Converg.*, 2024, **11**, 22.
30 O. E. Eremina, A. T. Czaja, A. Fernando, A. Aron, D. B. Eremin and C. Zavaleta, *ACS Nano*, 2022, **16**, 10341–10353.
31 D. B. Werz, R. Ranzinger, S. Herget, A. Adibekian, C. W. von der Lieth and P. H. Seeberger, *ACS Chem. Biol.*, 2007, **2**, 685–691.
32 C. Ilaria, B. Barbara, P. Arianna, C. Elena, M. Paola, V. Manuela, K. Evgenia, V. Davide and P. Alberto, *Semin. Cancer Biol.*, 2020, **62**, 9–19.
33 M. Michalczyk, E. Humeniuk, G. Adamczuk and A. Korga-Plewko, *Int. J. Mol. Sci.*, 2022, **24**, 103.
34 B. P. Toole, *Nat. Rev. Cancer*, 2004, **4**, 528–539.
35 K. Liu, A. K. M. A. Ullah, A. Juhong, C.-W. Yang, C.-Y. Yao, X. Li, H. L. Bumpers, Z. Qiu and X. Huang, *Small Sci.*, 2024, **4**, 2300154.
36 Y. Wang, J. E. Q. Quinsaat, T. Ono, M. Maeki, M. Tokeshi, T. Isono, K. Tajima, T. Satoh, S. I. Sato, Y. Miura and T. Yamamoto, *Nat. Commun.*, 2020, **11**, 6089.
37 X. Wu, L. Luo, S. Yang, X. Ma, Y. Li, C. Dong, Y. Tian, L. Zhang, Z. Shen and A. Wu, *ACS Appl. Mater. Interfaces*, 2015, **7**, 9965–9971.
38 I. Srivastava, R. Xue, J. Jones, H. Rhee, K. Flatt, V. Gruev and S. Nie, *ACS Nano*, 2022, **16**, 8051–8063.
39 M. P. Monopoli, D. Walczyk, A. Campbell, G. Elia, I. Lynch, F. B. Bombelli and K. A. Dawson, *J. Am. Chem. Soc.*, 2011, **133**, 2525–2534.
40 S. Okyem, O. Awotunde, T. Ogunlusi, M. B. Riley and J. D. Driskell, *Bioconjugate Chem.*, 2021, **32**, 1753–1762.
41 C.-W. Yang, K. Liu, C.-Y. Yao, B. Li, A. Juhong, A. K. M. A. Ullah, H. Bumpers, Z. Qiu and X. Huang, *ACS Appl. Mater. Interfaces*, 2024, **16**, 27055–27064.
42 I. Srivastava, R. Xue, J. Jones, H. Rhee, K. Flatt, V. Gruev and S. Nie, *ACS Nano*, 2022, **16**, 8051–8063.
43 K. Shimura and K. Kasai, *Anal. Biochem.*, 1995, **227**, 186–194.
44 C. E. Hayes and I. J. Goldstein, *J. Biol. Chem.*, 1974, **249**, 1904–1914.
45 *The Lectins: Properties, Functions, and Applications in Biology and Medicine*, ed. I. E. Liener, N. Sharon and I. J. Goldstein, Academic Press, Orlando, FL, 1986.
46 Y. Nagata and M. M. Burger, *J. Biol. Chem.*, 1974, **249**, 3116–3122.
47 V. P. Bhavanandan and A. W. Katlic, *J. Biol. Chem.*, 1979, **254**, 4000–4008.
48 M. Monsigny, A.-C. Roche, C. Sene, R. Maget-Dana and F. Delmotte, *Eur. J. Biochem.*, 1980, **104**, 147–153.
49 W.-J. Chen, K. Kandasamy and Y.-C. Chen, *ACS Appl. Nano Mater.*, 2019, **2**, 3348–3357.
50 C. L. Schofield, A. H. Haines, R. A. Field and D. A. Russell, *Langmuir*, 2006, **22**, 6707–6711.
51 D. Craig, J. Simpson, K. Faulds and D. Graham, *Chem. Commun.*, 2013, **49**, 30–32.
52 F. Wang, N. Sun, Q. Li, J. Yang, X. Yang and D. Liu, *J. Am. Chem. Soc.*, 2022, **145**, 919–928.
53 J. E. Hudak and C. R. Bertozzi, *Chem. Biol.*, 2014, **21**, 16–37.
54 C. R. Bertozzi and L. L. Kiessling, *Science*, 2001, **291**, 2357–2364.

55 R. A. Laine, *Glycobiology*, 1994, **4**, 759–767.
56 P. J. Hernando, S. Dedola, M. J. Marín and R. A. Field, *Front. Chem.*, 2021, **9**, 668509 and references cited therein.
57 K. El-Boubbou, D. C. Zhu, C. Vasileiou, B. Borhan, D. Prosperi, W. Li and X. Huang, *J. Am. Chem. Soc.*, 2010, **132**, 4490–4499.
58 K. El-Boubbou, C. Gruden and X. Huang, *J. Am. Chem. Soc.*, 2007, **129**, 13392–13393.
59 U. V. Sathisha, S. Jayaram, M. A. H. Nayaka and S. M. Dharmesh, *Glycoconjugate J.*, 2007, **2007**, 497–507.
60 M. W. Robertson, K. Albrandt, D. Keller and F.-T. Liu, *Biochemistry*, 1990, **29**, 8093–8100.
61 X. Li, S. Song, Q. Shuai, Y. Pei, T. Aastrup, Y. Pei and Z. Pei, *Sci. Rep.*, 2015, **5**, 1–9.
62 H.-J. Cho, *J. Pharm. Invest.*, 2020, **50**, 115–129.
63 C.-H. Whang, J. Hong, D. Kim, H. Ryu, W. Jung, Y. Son, H. Keum, J. Kim, H. Shin, E. Moon, I. Noh, H.-S. Lee and S. Jon, *Adv. Mater.*, 2022, **34**, 2203993.
64 I. Camby, L. M. Mercier, F. Lefranc and R. Kiss, *Glycobiology*, 2006, **16**, 137R–157R.
65 T. Funasaka, A. Raz and P. Nangia-Makker, *Glycobiology*, 2014, **24**, 886–891.
66 R. M. Neve, K. Chin, J. Fridlyand, J. Yeh, F. L. Baehner, T. Fevr, L. Clark, N. Bayani, J. P. Coppe, F. Tong and T. Speed, *Cancer Cell*, 2006, **10**, 515–527.
67 A. J. Minn, G. P. Gupta, P. M. Siegel, P. D. Bos, W. Shu, D. D. Giri, A. Viale, A. B. Olshen, W. L. Gerald and J. Massagué, *Nature*, 2005, **436**, 518–524.
68 J. Li, X. M. Zha, R. Wang, X. D. Li, B. Xu, Y. J. Xu and Y. M. Yin, *Biomed. Pharmacother.*, 2012, **2**, 144–150.
69 S. Fujisawa, K. Takagi, M. Yamaguchi-Tanaka, A. Sato, Y. Miki, M. Miyashita, H. Tada, T. Ishida and T. Suzuki, *Cancers*, 2024, **16**, 3600.
70 K. Nam, S. H. Son, S. Oh, D. Jeon, H. Kim, D. Y. Noh, S. Kim and I. Shin, *Oncotarget*, 2017, **8**, 35804.
71 S. N. D. Santos, H. Sheldon, J. X. Pereira, C. Paluch, E. M. Bridges, M. C. El-Cheikh, A. L. Harris and E. S. Bernardes, *Oncotarget*, 2017, **8**, 49484.
72 G. Zhang, X. Huang, Y. Gong, Y. Ding, H. Wang, H. Zhang, L. Wu, R. Su, C. Yang and Z. Zhu, *J. Am. Chem. Soc.*, 2024, **146**, 29053–29063.
73 K. G. Leslie, K. A. Jolliffe, M. Müllner, E. J. New, W. B. Turnbull, M. A. Fascione, V. P. Friman and C. S. Mahon, *Biomacromolecules*, 2024, **25**, 7466–7474.
74 Y. Xiang, J. Liu, J. Chen, M. Xiao, H. Pei and L. Li, *ACS Appl. Mater. Interfaces*, 2014, **16**, 15861–15869.
75 R. Kohavi, *Ijcai*, 1995, 1137–1143.
76 T. Hastie, R. Tibshirani and J. H. Friedman, *The elements of statistical learning: data mining, inference, and prediction*, Springer, New York, 2009.
77 B. D. Chithrani, A. A. Ghazani and W. C. Chan, *Nano Lett.*, 2006, **6**, 662–668.
78 M. Liu, Q. Li, L. Liang, J. Li, K. Wang, J. Li, M. Lv, N. Chen, H. Song, J. Lee and J. Shi, *Nat. Commun.*, 2017, **8**, 15646.
79 S. Rodal-Cedeira, S. Rodal-Cedeir, S. Vázquez-Arias, G. Bodelón, A. Skorikov, S. Núñez-Sánchez, A. Laporta, L. Polavarapu, S. Bals, L. M. Liz-Marzán, J. Pérez-Juste and I. Pastoriza-Santos, *ACS Nano*, 2020, **14**, 14655–14664.
80 A. Bajaj, O. R. Miranda, I. B. Kim, R. L. Phillips, D. J. Jerry, U. H. Bunz and V. M. Rotello, *Proc. Natl. Acad. Sci. U. S. A.*, 2009, **106**, 10912–10916.